

Polarization-dependent photocurrent in a quadrilateral-shaped bulk crystalline tellurium chip with near-infrared light excitation

Hiro Munekata^{1*}, Gakuto Kusuno¹, Kohei Miyazaki¹, and Takuya Satoh^{1,2*}

¹ *Department of Physics, Institute of Science Tokyo, Tokyo 152-8551, Japan*

² *Quantum Research Center for Chirality, Institute for Molecular Science, Okazaki 444-8585, Japan*

* E-mail: munekata.h.aa@m.titech.ac.jp; satoh@phys.sci.isct.ac.jp

ABSTRACT

A circular polarization-dependent photocurrent is exclusively observed along the direction parallel to the helical axis in millimeter-sized quadrilateral-shaped bulk crystalline tellurium samples. The deterioration of the polarization-dependent character of unclear origin is also recorded. The estimate of the gyrotropic photoconductivity constant β in the context of the circular photogalvanic effect yields the value of approximately 5 $\mu\text{A}/\text{W}$ based on experimental results obtained under a relatively weak excitation of 1.7 W/cm^2 . A comparison of this β value with those reported in previous studies is also discussed. Enhancement of β value may be achievable with bulk samples of superior crystalline quality.

Keywords:

photo-galvanic effect, circular polarization, Te crystal, spin non-degenerate bands, photo-induced deterioration

I. INTRODUCTION

Let us imagine a spiral wire, along which tellurium (Te) atoms are placed regularly in such a way that the fourth Te atom lies directly on the first Te atom, namely, a long, trigonal wire made of Te atoms [Fig. 1(a)].¹⁾ The number of such wires condense into a hexagonal array [Fig. 1(b)], with the axis of the spiral wire, *the helical axis*, parallel to the direction of the pillar of a hexagonal prism, the z axis [Fig. 1(c)]. Although the Te crystals take the form of hexagonal prisms, they have a three-fold symmetry, as shown in Fig. 1(b).

Experimental studies on the electronic and optical properties and device applications of Te crystals and films were conducted primarily in the 1960s to 1970s: central motivation being the elucidation of the energy band structure, understanding its exotic physical properties, and its applications in solid-state devices. Representative experimental studies include, but are not limited to, infrared absorption spectroscopy,²⁻⁴⁾ cyclotron resonance,⁵⁾ crystal-axis-dependent carrier transport,⁶⁾ and thin-film transistors.^{7,8)} Bulk Te crystals should be regarded as three-dimensional electronic systems.⁶⁾ The fundamental concept of optical memory has been established through studies using Te-based films.⁹⁻¹¹⁾

The work with the tight binding scheme along a spiral wire has opened a theoretical consideration of energy bands for this type of crystal.¹²⁾ Group theoretical methods have been introduced to account for energy spectra in connection with a few different symmetry points in the Brillouin zone.¹³⁾ These two studies were followed by calculations of energy bands with various theoretical treatments in 1966 and 1967, through which the presence of an energy gap around the H point of the Brillouin zone was clarified. The remaining problem of valence band structures, either single maximum or double maxima, has finally clarified by very careful calculations using the group theory and the $\mathbf{k}\cdot\mathbf{p}$ perturbation method¹⁴⁻¹⁶⁾ involving severe comparison with experimental results.⁵⁻⁷⁾ Through these theoretical studies, the double-band maximum accompanied by *non-degenerate* spin states, in other words, *non-degenerate* states of the total angular momentum has finally been established for the top part of the valence band. A critical review of prior theoretical studies is available in Ref. 14.

A new photogalvanic effect (PGE) induced by optical excitation with circularly polarized light in a chiral crystal, such as a Te crystal, was suggested in the late 70's,¹⁷⁾ presumably after careful study of the theoretical works mentioned in the previous paragraph. The experiments were performed to determine photo-induced electromagnetic force (emf) across crystalline Te rods using circularly polarized, pulsed infrared light excitation.^{18,19)} The emf of 0.2–1.0 mV was observed in p -type Te samples along the z axis with the 100-ns pulse excitation and peak power of 3 kW at 10.6 μm wavelength of a Q-switch CO₂ laser. This

excitation condition involves Raman-type virtual excitation consisting of two steps: indirect absorption and direct emission around the H point.¹⁹⁾

Interest in searching a Weyl semimetal, a system incorporating three-dimensional Dirac cones without spin degeneracy around the Fermi level,²⁰⁾ has led theoretical researchers to shed light again on Te and Se crystals.^{21,22)} Experimental studies have also been invoked in view of modern spin-related phenomena, as represented by current-induced magnetization in a bulk Te crystal,^{23,24)} electrical magneto-chiral anisotropy,²⁵⁾ circular PGE (CPGE) photocurrents in Te flakes,^{26,27)} and polarized-infrared/terahertz photocurrents in bulk Te crystals²⁸⁾ that have been regarded different from the conventional PGEs.¹⁹⁾

Through the study of the interaction between light and solids, more specifically, the interaction between circularly polarized light and spin/phonon sub-systems,²⁹⁻³¹⁾ we developed a strong interest in chiral systems because they would couple relatively strongly with the circular polarization (CP) of light.^{32,33)} Based on the previous studies on Te crystals, we infer that these types of crystals with unique structures would be suitable for studying the photogeneration of a spin-polarized current, as well as CP photodetectors³⁴⁾ and emitters.³⁵⁾

In the present work, we focus on the shape-controlled, bulk Te crystals and the detection of CPGE in these samples. It would be quite challenging to rely only on Te flakes for systematic studies of physical properties and future device applications because they lack flexibility in controlling their size, shape, and crystal orientations. With this in mind, we have prepared quadrilateral-shaped, millimeter-sized bulk Te chips with metallic electrodes to study a polarization-dependent PGE. The experimental data strongly suggest the occurrence of a CPGE, which reflects the gyrotropic character of a Te crystal. However, deterioration of the polarization-dependent character of unclear origin has also been observed. Nevertheless, it is encouraging that such a coherent process of light-matter interaction can be detected at a distance of millimeters between the excitation region and electrodes.

In addition, inverse analysis with a phenomenological equation for CP-dependent photocurrent has been carried out, and relative magnitude of the CPGE component was estimated to be approximately 1% relative to the background of polarization-independent photocurrent. Furthermore, based on discussions in terms of third-rank gyrotropic photoconductivity tensors that reflect the crystal point group of trigonal Te, D_3 , the efficiency of the CPGE and the value of the gyrotropic photoconductivity tensor β ³⁶⁾ were estimated using the experimental data obtained under a relatively weak excitation of 1.7 W/cm².

II. MATERIALS

A Te lump (purity 4N) was first cleaved into 5–15 mm large, 0.5–2 mm thick, mother pieces. The pieces were then characterized using a multi-purpose θ - 2θ X-ray diffractometer (D8 DISCOVER, Bruker; X-ray source Cu-K α 1.541 Å), and in-plane and out-of-plane crystal axes were identified. The area of X-ray irradiation on the sample is estimated to be approximately 1.9 mm \times 0.4 mm at the Bragg's angle of $\theta_B \sim 22^\circ$.³⁷⁾ It is worth noting that X-ray diffraction (XRD) detects a Te crystal as a crystal with *six-fold symmetry*, where spacings and directions of periodic reflection planes; namely, {100} and {010} are equivalent. Reflection planes and their directions are specified on the basis of Miller indices, as shown in Fig. 1(c): namely, **a** \parallel [100], **b** \parallel [010], and **c** \parallel [001], whereas direction normal to the (010) plane is **y** \parallel [120]. Superimposing the orthogonal crystal coordinate system, we see [100] \parallel **x**, [120] \parallel **y**, and [001] \parallel **z**, respectively.

Figures 2(a) and (b) show two pole figures obtained at the Bragg's angles of $2\theta_B = 22.8$ – 23.4 and 27.4 – 28.0° , respectively,³⁷⁾ for one of the mother pieces [Fig. 2(c)]. The former is the reflection from the {010} plane, whereas the latter is the reflection from the {011} plane. Shown in Fig. 2(c) is a top view of the mother Te piece, on which an X-ray beam is impinged from the three o'clock directions ($\varphi = 0^\circ$) with an incident angle $\omega (\equiv \theta_B)$. The symbols φ and ψ in the pole figures represent the in-plane rotation and tilt angles of the sample stage, respectively, with respect to the incident X-ray plane. The measurement configurations for $\varphi = 0^\circ$ and 90° are shown schematically in Figs. 2(d) and (e), respectively.

The elongated bright spot centralized at $(\varphi, \psi) = (0, 0)$, spot *a* in Fig. 2(a), indicates that the (010) plane lies parallel to the sample surface, which is consistent with the previous studies on cleaved planes.^{1,38)} The elongation along the radial direction indicates that reflection from the (010) plane involves a dispersion of approximately 10° along the direction orthogonal to the plane of X-ray incidence ($\varphi = 0^\circ$). Spots *b* and *c* in Fig. 2(a) are the reflection obtained from both neighboring planes of the (010) plane, namely $(\bar{1}10)$ and (100), respectively.

Rotating and tilting the sample at the Bragg's angle of $2\theta_{\text{XRD}} = 27.7^\circ$ give rise to the observation of a series of reflection from the {011} planes; e.g., representative spots, *d*, *e*, and *f* at $(\varphi, \psi) = (270^\circ, 65^\circ)$, $(37^\circ, 65^\circ)$, and $(127^\circ, 65^\circ)$ in Fig.2(b) correspond to the

reflection from the (011), ($\bar{1}11$), and (101) planes, respectively. The observed pattern indicates that the [001] direction is along $\varphi = 0^\circ$ which is parallel to the X-ray incidence plane. The elongation in these spots indicates a dispersion of approximately 10° along the direction orthogonal to the plane of X-ray incidence ($\varphi = 90^\circ$); for instance, the 10° dispersion of the [001] direction in the case of spot *d*.

The XRD data from different points on the mother Te chip qualitatively exhibited the same patterns as those shown in Figs. 2(a) and (b). To summarize these two pole figures, the direction normal to a sample surface is $[120] \parallel \mathbf{y}$, whereas the direction parallel to a long side is $[001] \parallel \mathbf{z}$. Naturally, the direction parallel to a short side is $[100] \parallel \mathbf{x}$. Dispersion of around 10° indicates disorders of crystalline planes in terms of macroscopic orientation and of microscopic spatial distance between the planes. The in-plane and out-of-plane distributions of these disorders have not yet been clarified.

III. DEVICE FABRICATION

Mother pieces that clearly exhibited an in-plane *z* axis were selected for device fabrication. Selected pieces were cut into quadrilateral-shaped, millimeter-sized Te chips with great care to take on near-rectangular shapes with their sides either parallel or perpendicular to the *z* axis. This process was carried out under a stereomicroscope using jewelry processing tools, such as a microstring saw and a microfile. A successful example is shown in Fig. 3(a). During the CPGE experiments on the *as-cleaved* devices, we observed deterioration of the polarization-dependent photocurrent. This prompted us to study the suppression of deterioration concurrently with CPGE. It has been inferred that photo-induced oxidation and subsequent amorphization of a crystalline Te surface occurred.³⁹⁾ For this purpose, devices with mirror-polished and SiO₂-coated surfaces were prepared in addition to those with *as-cleaved* surfaces. The process of surface polish and SiO₂-coating, which is relatively simple and free from conventional chemical lithography, is described in the next paragraph.

Figures 3(b) and (c) show schematic illustrations of the device from the top and cross-sectional views, respectively. First, the chip was mounted on a cover glass with an epoxy-based adhesive, with the *as-cleaved* {010} plane facing upward. The area surrounded by the red lines in Figs. 3(b) and (c) represents the area of the epoxy. Second, the sample surface was mirror polished using a mixture of alumina powder and a nonaqueous solvent, and the

resultant sample thickness was unified at approximately 300 μm . No post-polishing chemical etching was performed. This was followed by electrode formation: metal fingers were applied on each side of a chip with silver paste or a mixture of gold-silver paste, and aluminum (Al) wires of 100- μm diameter were bonded to the end of the fingers. Two- and four-finger devices were fabricated. Finally, the as-prepared devices were coated with a 300-nm thick amorphous SiO_2 layer by RF sputtering.⁴⁰⁾ The regions surrounded by green lines correspond to the SiO_2 layer. Photographs of the actual two- and four-terminal devices are presented in inset Fig. 4(a) and Fig. 5(a), respectively. For devices with *as-cleaved* surfaces, the second and final steps are omitted.

Overall, more than ten devices were prepared and tested to determine whether they exhibited a photocurrent worth studying for the PGE. Two representative experimental results, obtained from the two-finger device (sample A) and the four-finger device (sample B), are presented in Sections VI (1) and (2), respectively.

IV. RAMAN SCATTERING

Raman scattering characterization was carried out to study the possible damage caused by RF sputtering of SiO_2 -coated devices. Experiments on light-induced oxidation³⁹⁾ were also performed. Raman spectra were measured in a standard backscattering configuration at room temperature in an air atmosphere using a semiconductor laser with a wavelength λ of 785 nm and a power of 7 mW (density 50 kW/cm^2). Figure 4(a) shows the Raman spectra obtained from *SiO₂-coated* sample A. Depending on the Raman excitation selection rule, the two lines at 124 and 144 cm^{-1} are clearly identified as A_1 and E phonon modes.^{32,41)} This indicates that the device surface is not severely damaged by the process of SiO_2 coating and has single crystalline features. Figure 4(b) shows the Raman data in relatively high wavenumber region (400–800 cm^{-1}). This region is important because early researchers have reported the inducement of TeO_x layers in the regions represented by yellow zones in the figure, during the illumination of a CW-laser beam ($\lambda = 441.6, 488.0, \text{ and } 514.5 \text{ nm}$, 0.1–100 kW/cm^2) in an air atmosphere.³⁹⁾ Fortunately, the occurrence of oxides was not observed within the limit of illumination at $\lambda = 785 \text{ nm}$ and exposure time up to 92 min. It appears that the SiO_2 layer prevented the light-induced oxidation and subsequent amorphization of the Te underlayer region.

V. PHOTOCURRENT MEASUREMENT

A sample was mounted on a vertical, sample rod in an aluminum sample box in such a way that $[120] \parallel y$ direction was parallel to the sample normal and $[001] \parallel z$ direction pointed horizontally. Naturally, $[100] \parallel x$ direction pointed vertically. The sample was rotated around the $[100]$ axis at a tilt angle θ relative to the $[120]$ direction. A picture of sample B mounted in the box is shown in Fig. 5(a), along with a schematic illustration of the relationship between the direction of the Miller indices and the orthogonal coordinate system (x, y, z) . Hereafter, the latter coordinate system is used primarily to describe the experimental results and discussions in subsequent sections.

Excitation was carried out with a CW semiconductor laser beam at $\lambda = 780$ nm and a power density in the range of 1.7–80 W/cm², which was controlled by the output power of the laser, neutral-density filters, and spot diameters of either approximately 40 or 100 μm . Details of excitation are specified in the experimental data presented in the next section.

A schematic diagram of the experimental setup is shown in Fig. 5(b). The penetration depth of light was estimated to be 20–50 nm at room temperature, referring to the absorption spectra measured by earlier researchers.³⁾ A zero-bias photocurrent was measured at room temperature in an air atmosphere with different tilt angles θ . The lock-in technique with a beam chopper operating at 163 Hz was used. A quarter wave plate (QWP) was rotated continuously during measurements, and a photocurrent as a function of rotation angle (φ_Q) of QWP was obtained. The linear polarizations (LPs) of a laser beam parallel and perpendicular to the x axis are defined as s and p polarizations, respectively.

CP-dependent artifacts in our measurement setup were examined using a polycrystalline Cu(In,Ga)Se₂ solar cell.⁴²⁾ The difference in the photocurrent between two opposite CP states, left CP (LCP) and right CP (RCP), was as small as $5 \pm 2 \times 10^{-4}$ relative to the photocurrent averaged over one QWP rotation (see Fig. 1S). This verified that our measurement setup was nearly free from artifacts caused by LCP and RCP excitations. We set the criterion in the present study that CP dependent photocurrent is present in a sample when the difference in photocurrent between LCP and RCP states is 1% or higher relative to the photocurrent averaged over one QWP rotation.

Figure 5(c) shows a schematic illustration of a model that relates the photocurrent (I_{ph} in A) to the current density (J in A/cm²). Here, the current is generated in the excitation region in the unit of cm³ and collected by a pair of electrodes adjacent to the excitation region. A

photocurrent flowing in a specific direction is assumed to pass through a cross-sectional window defined by the representative width of the excitation region and the penetration depth of light, and to be collected by a pair of electrodes placed outside the windows. This is a simplified model in that the photocurrent flowing through the window is collected without any dissipation or reduction. This model is applied in Section VI (3) to estimate the efficiency of the CPGE and a gyrotropic photoconductivity tensor.

VI. RESULTS and DISCUSSION

(1) Sample A

We first show zero-bias photocurrent (I_{ph}) data obtained from *as-cleaved* sample A: it has quadrilateral shape with the size around $1.5 \text{ mm} \times 0.8 \text{ mm}$, attached with a pair of electrodes separated approximately 0.7 mm along the z axis [inset Fig. 4(a)]. The linearity of current-voltage curves and the response under light illumination with various excitation conditions were tested for 1–2 h with normal incidence ($\theta = 0^\circ$) prior to the experiments on PGE. The sample exhibited ohmic characteristics with resistance around $1.5 \text{ k}\Omega$, and the magnitude of I_{ph} value was approximately $0.8\text{--}0.9 \text{ nA}$ when central part of the area $A = 1.26 \times 10^{-3} \text{ cm}^2$ was excited by a laser beam of 50.5 mW at normal incidence ($\theta = 0^\circ$). The power density under these condition was 40.1 W/cm^2 .

Tilting the device around the x axis led to a polarization-dependent photocurrent. Figure 6(a) shows the I_{ph} data as a function of QWP angle (φ_Q) obtained after the accumulated illumination time of $t = 2 \text{ h}$ with the tilt angle of $\theta = 45^\circ$. Excitation was kept at 40.1 W/cm^2 , with the initial polarization of p -polarization at $\varphi_Q = 0^\circ$. Two distinct features are observed: first, the $4\varphi_Q$ periodicity which reflects alteration of I_{ph} values between LP and CP, and second, modulation with the $2\varphi_Q$ periodicity at two different CP states, LCP and RCP, as pointed by green arrows in the figure. These facts are reminiscent of both linear PGE (LPGE) and CPGE reported by early researchers.^{19,26,27} The I_{ph} value at the LCP was larger than that at the RCP. The difference in I_{ph} between LCP and RCP excitation, ΔI_{ph} , is 0.0082 nA , indicating a modulation of 3.4% relative to the average I_{ph} value of 0.24 nA . It is quite encouraging that such a coherent process of light-matter interaction is observed through the measurement across a distance on the order of millimeters, in which various inelastic carrier scattering processes are involved.

A reduction in ΔI_{ph} values was observed under repeated experiments. However, some

local spots retained the CP-dependent I_{ph} , as shown in Fig. 6(b), which shows the data obtained after $t = 7$ h. Further repeating experiments resulted in a somewhat unstable I_{ph} and a loss of polarization-dependent characteristics, as shown in Fig. 6(c), which was obtained after $t = 11$ h.

The observed light-induced deterioration led us to suspect that the sample underwent photo-induced oxidation and amorphization.³⁹⁾ To address this problem, the light-illuminated surface of the *as-cleaved* sample A was removed by a mirror polishing process, and its polished surface was then coated with amorphous SiO_2 layers. The surface condition of *SiO₂-coated* device A was evaluated together with *in-situ* monitoring of oxidation by Raman scattering, as described in Section IV.

The photocurrent in the regenerated *SiO₂-coated* sample A decreased by one order of magnitude compared to that of the fresh *as-cleaved* sample A. This suggests an increase in the density of the surface recombination centers, presumably resulting from polishing and SiO_2 coating. Nevertheless, the recovery of the polarization-dependent photocurrent is clearly observed (see Fig. 2S), as evidenced by the data obtained after an accumulated illumination time t of approximately 6.5 h with an excitation power density of 44.5 W/cm^2 . The magnitude relation of the I_{ph} values between the LCP and RCP is the same as that observed in the *as-cleaved* sample A.

With further continuous measurements, the fluctuations in the photocurrent gradually became pronounced, and the polarization-dependent characteristics gradually deteriorated and were completely lost after $t = 13$ h. However, the reduction in the average photocurrent was not obvious. Considering the Raman data shown in Fig. 4(b), the observed degradation may not be simply due to light-induced oxidation.

(2) Sample B

The results of experiments with sample A led us to an attempt to circumvent the unknown deterioration of the CP-dependent photocurrent by reducing the illumination power. We now turn our attention to the experimental results obtained from device B that was cut from another mother piece and was different from device A. The lengths of short and long sides were 0.7 and 0.9 mm, respectively. The former is parallel to the x direction, whereas the latter is parallel to the z direction. Two pairs of electrodes were formed, namely pairs 2–3 parallel to the x axis and pairs 1–4 parallel to the z axis. A photograph of this device is shown in Fig. 5(a). The φ_Q -dependent I_{ph} data measured before the SiO_2 coating exhibited relatively large photocurrent and clear CP-dependent photocurrent [graphical data omitted].

Figure 7(a) shows the I_{ph} data for the *SiO₂-coated* sample B, which was measured along the z direction through pairs 1–4 after an accumulated illumination time of $t = 5.5$ h. The initial polarization state at $\varphi_Q = 0^\circ$ was linear p -polarization. Taking precautions against the deterioration of the polarization-dependent photocurrent, the excitation power was reduced to 2.1 mW while maintaining the same excitation area of $A = 1.26 \times 10^{-3} \text{ cm}^2$. Consequently, the power density reduced to 1.7 W/cm^2 , and I_{ph} decreased accordingly. The data obtained at normal incidence ($\theta = 0^\circ$) slightly show the $4\varphi_Q$ periodicity. Tilting the device around the x axis gives rise to enhanced I_{ph} together with much pronounced $4\varphi_Q$ dependence, as represented by the data obtained at $\theta = 45^\circ$. The φ_Q dependence will be discussed later in the next section. Most importantly, modulation with the $2\varphi_Q$ periodicity is superimposed on the $4\varphi_Q$ dependence, as pointed with green arrows in the figure. Interestingly, the magnitude relationship of I_{ph} between the LCP and RCP was the same as that in sample A.

Figure 7(b) shows the I_{ph} data measured along the x direction through pairs 2–3, which are perpendicular to the z axis. Magnitudes of photocurrent are smaller on the whole, and both $4\varphi_Q$ and $2\varphi_Q$ periodicities hide in a shadow, leaving I_{ph} profiles rather cloggy. This indicates the presence of a strong in-plane anisotropy in the photocurrent in z and x directions.

These observations lead us to the conclusion that CP-dependent photocurrent can clearly be detected along the z direction even in handmade millimeter-sized devices whose size and shape are engineered by mechanical means. For both samples, excitation with LCP yielded a larger photocurrent than excitation with RCP, which suggests that the source Te lump consists of a single helicity. Dependence of the helicity in the Te crystal on the magnitude relation of the CP-dependent photocurrent will be the subject of a future study.

We note that the deterioration of polarization-dependent characteristics occurred again for *SiO₂ coated* sample B, even under relatively weak excitation conditions. In this particular case, the photocurrent gradually decreased as the accumulated illumination time t increased, and it became comparable to the resolution limit of approximately 1 pA after around $t = 13$ h. Before the state of complete deterioration, CP-dependent characteristics were barely noticeable, as shown in Fig. 3S for I_{ph} data measured after an accumulated illumination time $t = 10$ h with s -polarization. It is interesting to note that, although the phase of entire $4\varphi_Q$ modulation is reversed in the case of s -polarization excitation, magnitude relation between LCP and RCP states is preserved. This will be discussed in the next section.

Based on the Raman scattering data shown in Fig. 4, the observed deterioration in CP-dependent I_{ph} cannot be attributed to light-induced oxidation and subsequent

amorphization.³⁹⁾ We infer that the deterioration may originate from an increase in the number of photocarrier trapping sites, which affects the non-equilibrium population of photocarriers in *spin-non-degenerate* states near the band gap. We believe that the deterioration may be significantly suppressed in bulk samples with superior surface/crystalline quality.

(3) Discussion

The observed anisotropic zero-bias photocurrent strongly suggests that they can be attributed to the PGE involving the crystal symmetry of Te. In general, the phenomenological optical response can be represented by third-rank tensors.³⁶⁾ We formulated the relationship between the optical excitation power and the resultant anisotropic photocurrent in the Te crystal by considering the crystal point group of D_3 ,⁴³⁾ which resulted in a nonzero conductivity tensor:

$$\sigma_{yyx} = \sigma_{yxy} = \sigma_{xyy} = -\sigma_{xxx}$$

$$\sigma_{xyz} = -\sigma_{yxz}$$

$$\sigma_{xzy} = -\sigma_{yzx}$$

$$\sigma_{zxy} = -\sigma_{zyx}$$

Note that tensors consist of real and imaginary parts,⁴⁴⁾ $\sigma_{ijk} = \sigma'_{ijk} - i\sigma''_{ijk}$.

Starting from the general expression of $J_i = \sigma_{ijk} E_j E_k^*$, equations of anisotropic photocurrent densities for the experimental configuration with p -polarization at $\varphi_Q = 0^\circ$ are expressed by Eqs. (1) to (4). For $\mathbf{J} \parallel \mathbf{z}$, the component due to the LPGE, J_{LPGE} , vanishes, whereas the component attributed to the CPGE, J_{CPGE} , remains: namely,

$$J_{\text{CPGE}} = -2\sigma''_{zyx} \sin \theta \sin 2\varphi_Q \quad (1)$$

$$J_{\text{LPGE}} = 0 \quad (2)$$

For $\mathbf{J} \perp \mathbf{z}$, the relation between LPGE and CPGE is changed as follows:

$$J_{\text{CPGE}} = 0 \quad (3)$$

$$J_{\text{LPGE}} = \frac{\sigma'_{xyy}}{4} \{(\sin \theta)^2 (\cos 4\varphi_Q + 3) + \cos 4\varphi_Q - 1\} - \frac{(\sigma'_{xzy} + \sigma'_{xyz})}{4} \sin 2\theta (\cos 4\varphi_Q + 3) \quad (4)$$

In these equations, the strengths of fields E_m and E_n , and thus $E_m E_n^*$ in the units of W/cm^2 , are regarded as unity; whereas J_i is a current density in the units of A/cm^2 . Note that the J_{CPGE} is rather simple in the case $\mathbf{J} \parallel \mathbf{z}$, whereas the J_{LPGE} is rather complicated in the case of $\mathbf{J} \perp \mathbf{z}$. In the case of s -polarization, relation between J_{CPGE} and φ_Q shifts 90° ,

and sign of RHS of Eq. (1) can be reversed: Naturally, the magnitude relationship between the excitation with LCP and RCP is unchanged, which can be verified through the data shown in Fig. 7(a) and Fig. 3S.

In practice, the photocurrent along the z direction can be expressed phenomenologically using four terms, as expressed by Eq. (5).⁴⁵⁾

$$I_{\text{ph}} = C \sin 2\varphi_Q + L_1 \sin 4\varphi_Q + L_2 \cos 4\varphi_Q + D \quad (5)$$

Here, the first and second terms correspond to the CPGE and LPGE, respectively, whereas the third and fourth terms are associated with the polarization-dependent absorption/reflection and polarization-independent terms caused by the difference in electrochemical potential between the illuminated and unilluminated regions, respectively. The third and fourth terms are not relevant to point group D_3 .

Figure 8(a) shows the results of numerical fitting of the experimental I_{ph} data shown in Fig. 7(a). The fitting yielded $C \sim 0.18$ pA, $L_1 \sim -0.18$ pA, $L_2 \sim 0.98$ pA, and $D \sim 13$ pA, with significant figures of two. We notice a relatively large contribution of the non- D_3 terms, the L_2 and D terms, whereas the contributions of the C and L_1 terms, both being PGE terms, are relatively small. A breakdown of the numerical fitting for each φ_Q -dependent term in Eq. (5) is shown in Fig. 8(b), which facilitates the determination of the contribution of each term. The most notable L_2 term can qualitatively be explained in terms of LP-dependent absorption of crystalline Te: the absorption coefficient is larger for light polarization parallel to the z axis ($\mathbf{E} \parallel \mathbf{z}$) than that for $\mathbf{E} \perp \mathbf{z}$.³⁾ Thus, photocurrent is largest when p -polarization light is impinged on Te at $\varphi_Q = 90^\circ n$ ($n = 0, 1, 2, \dots$), whereas it is smallest when CP light is impinged at $\varphi_Q = 45^\circ (2n + 1)$ ($n = 0, 1, 2, \dots$) where the p -polarization component is reduced by half. The polarization-dependent dielectric constant⁴⁶⁾ also helps to increase the difference in the photocurrent between the two polarization states. Within the context of polarization-dependent absorption scenario, magnitude relation in photocurrent between $\varphi_Q = 90^\circ n$ and $\varphi_Q = 45^\circ (2n + 1)$ is inverted when s -polarization is used for excitation (Fig. 3S). Therefore, L_2 term in Eq. (5) can be classified as a polarization-dependent first-order effect associated with the light absorption.

Let us now examine the validity of the nonzero L_1 and C coefficients. These values are smaller than the L_2 value, reflecting their higher-order characteristics. A careful inspection of Fig. 8(b) leads us to recognize the unique contributions of L_1 and C terms. First, the contribution of the L_1 term manifests as a slight asymmetrical distortion superimposed on the cosine waveform of the L_2 term. This suggests that small fluctuations in the photocurrent

may result in a nonzero L_1 coefficient, and one must be careful when dealing with small L_1 values. It is difficult to determine the contribution of the L_1 term solely from experimental data obtained in the present study.

In contrast, contribution of the C term is rather straightforward: it manifests itself as a periodic amplitude modulation at $\varphi_Q = 45^\circ (2n + 1)$, which is relatively easy to read from experimental data when background signals are reasonably stable. We can recognize these points in Figs. 4S(a) and (b), in which calculations without the L_1 and C terms are shown, respectively. Consequently, we may be able to state that validity of C coefficient is relatively higher than that of the L_1 coefficient.

Table 1 summarizes the values of the four coefficients obtained by fitting the experimental data to Eq. (5). It is clear that the polarization-independent D term decreases with either photodeterioration or surface polishing. Interestingly, the ratio C/D remains nearly constant, 0.01–0.02, for both samples A and B no matter excitation is relatively weak or strong. The range of the ratio L_2/D is a little wide, 0.04–0.09, for which the difference in reflection due to surface roughness may be responsible. In case of excitation with s -polarization, polarities of C and L_2 are reversed. However, the magnitude relation in the photocurrent between the LCP and RCP excitations remains unchanged, as expected.

Analyses of the photocurrent data obtained along the x direction at $\theta = 0^\circ$ (normal incidence) were also carried out using the data shown in Fig. 7(b). At $\theta = 0^\circ$, Eq. (4) is simplified as $I_{ph} - D = J(\perp \mathbf{z}) \cdot A' = L_1'(\cos 4\varphi_Q - 1)$, where $L_1' = \frac{\sigma'_{xyy} \cdot A'}{4}$ with A' the area of cross section through which a current flows [Fig. 5(c)]. The quantity $I_{ph} - D$ can be obtained from the difference between the maximum and minimum photocurrents, I_{\max} and I_{\min} , at $\varphi_Q = 90^\circ n$, ($n = 0, 1, \dots$) and $\varphi_Q = 45^\circ(n + 1)$, ($n = 1, 3, \dots$), respectively. The averaged values are $I_{\max} = 4.63$ pA and $I_{\min} = 4.57$ pA, from which L_1' of 0.06 pA is estimated. This suggests that the effect of LPGE on Te was not significant.

Based on the C value extracted from the data shown in Fig. 7(a) for SiO_2 -coated sample B, the efficiency of CPGE is estimated to be around 1.1×10^{-13} A·cm²/W with the excitation power density of 1.7 W/cm². With this value, we are able to estimate the value of $2\sigma''_{zyx}$ in Eq. (1) using the simplified model presented in Section V and Fig. 5(c). Note that $2\sigma''_{zyx}$ is tied together with the gyrotropic conductivity tensor β through $\beta_{ij} = \varepsilon_{jkl} \text{Im}\{\sigma_{ikl}\} = -\varepsilon_{jkl} \sigma''_{ikl}$ in which β_{ij} is the second-rank axial tensor, ε_{ijk} the third-rank Levi-Civita tensor, and σ_{ikl} the third-rank polar tensor.⁴⁴⁾ The area of the cross-sectional window A' is

estimated by the diameter of excitation spot ϕ multiplied by the penetration depth of light d , that is, $A' = 40 \mu\text{m} \times 50 \text{nm} = 2 \times 10^{-8} \text{cm}^2$. Then, $2\sigma''_{zyx} = \frac{1 \times 10^{-13} \text{A}\cdot\text{cm}^2/\text{W}}{2 \times 10^{-8} \text{cm}^2} = 5 \times 10^{-6} \text{A}/\text{W} = 5 \mu\text{A}/\text{W}$, with one significant figure. Theoretical considerations in the case of intra-band excitation⁴⁷⁾ have suggested a β value of approximately $2 \mu\text{A}/\text{W}$ at room temperature for p -type Te with hole concentrations of mid 10^{14} to high 10^{15}cm^{-3} . An estimation of the β value in the case of *inter-band* excitation is not available at the present stage.

Let us briefly review the magnitudes of CPGE obtained by early researchers.^{26,27)} Experiments of PGE with p -type, Te flakes of a few tens- μm excited by a CW CO_2 laser at the wavelength $\lambda = 4.0, 4.5,$ and $10.6 \mu\text{m}$ determined CPGE of approximately 1.4nA at $680 \text{W}/\text{cm}^2$ *only* in experiments with $\lambda = 10.6 \mu\text{m}$, which corresponds to the efficiency of $1.8 \times 10^{-12} \text{A}\cdot\text{cm}^2/\text{W}$ ²⁶⁾ and $\beta \sim 180 \mu\text{A}/\text{W}$ based on our model. The authors suggested that CPGE occurs only via an intrinsic second-order process, which confirms the experiments carried out in the 70's.¹⁹⁾ However, their experimental findings suggested that a direct band-to-band transition around the H point did not yield CPGE.

Experiments of CPGE involving inter-band transition with p -type Te flakes of size around $100 \mu\text{m}$ excited by a CW-laser at $\lambda = 633 \text{nm}$ up to the power of 0.6mW have yielded CP photocurrent of $10.9 \text{nA}/\text{mW}$, which corresponds to the efficiency of $4.1 \times 10^{-12} \text{A}\cdot\text{cm}^2/\text{W}$ referring the diameter of an excitation spot of around $7 \mu\text{m}$.²⁷⁾ The value of β is estimated to be $1200 \mu\text{A}/\text{W}$ based on our model. The authors suggested that a two-dimensional effect modified the band structure and resulted in a CPGE in the visible wavelength region. However, the thickness of the Te flakes was not reported. In any case, the contribution of two-dimensional effect would be remote in the studies using bulk-type Te. In the bulk, the energy band structure close to that of a Weyl semimetal²⁰⁻²²⁾ might exist in the k -space that is relatively far from the H point. We assume that the relatively large efficiencies obtained in Te flakes^{26,27)} are presumably due to their superior crystalline quality.

Enhancement of the efficiency of the CPGE might also be possible by suppressing the non-polarization-dependent photocurrent, the fourth term in Eq. (5). The driving force of the fourth term originates from the difference in the electrochemical potential between the excited and non-excited areas. Homogeneous excitation throughout the entire sample surface may lead to a reduced polarization-independent photocurrent. Applying a small DC current that compensates for the polarization-independent photocurrent is another interesting option. The contribution of the C value relative to the entire photocurrent can also be enhanced by

controlling the surface roughness and crystal quality.

VII. CONCLUSIONS

We have prepared various quadrilateral-shaped single-crystal Te samples of millimeter size and have experimentally studied the polarization-dependent photocurrent in these samples in view of PGE. CP-dependent photocurrent has been observed exclusively along the direction parallel to the helical (z) axis. Unforeseen deterioration of the polarization-dependent characteristics has also been observed with an increase in the accumulated illumination time. Surface protection with the SiO_2 coating has not completely suppressed the observed deterioration, which suggests that the observed deterioration cannot be attributed to photoinduced oxidation. Despite of such situation, inverse analysis with a phenomenological equation for CP-dependent photocurrent has been carried out, and relative magnitude of the CPGE component is estimated to be approximately 1% relative to the polarization-independent photocurrent. Furthermore, we have attempted to estimate the gyrotropic constant β by utilizing the third-rank photoconductivity tensor derived for crystal point group D_3 . A β value of approximately $5 \mu\text{A}/\text{W}$ has been estimated based on the efficiency of the CPGE ($1.1 \times 10^{-13} \text{ A}\cdot\text{cm}^2/\text{W}$) obtained under relatively weak excitation conditions. These values are smaller than those obtained by previous researchers using single-crystal Te flakes. We believe that a higher CPGE efficiency can be achieved with bulk samples of superior crystalline quality.

SUPPLEMENTARY MATERIALS

Posted are experimental data concerning the validation of photocurrent measurement setup (Fig. 1S), photocurrent data obtained from regenerated sample A (Fig. 2S) and from sample B before the stage of complete deterioration (Fig. 3S), and inverse analysis with incomplete phenomenological equations (Fig. 4S). These materials reinforce the rationality of our study.

ACKNOWLEDGEMENTS

We gratefully acknowledge Materials Analysis Division and Semiconductor and MEMS

Processing Division, both in the Core Facility Center at Institute of Science Tokyo, for x-ray diffraction measurements and RF sputtering of SiO₂ layers, respectively. We thank A. Iwase and Y.-C. Huang, student members in Satoh laboratory, for theoretical discussions and technical assistances. This work is supported in part by JSPS KAKENHI (Grant Nos. JP21H01032 and JP22H01154), MEXT X-NICS (Grant No. JPJ011438), NINS OML Project (Grant No. OML012301), and JST CREST (Grant No. JPMJCR24R5).

REFERENCES

- 1) A. Koma, E. Takimoto, and S. Tanaka, *Phys. Stat. Solidi* **40**, 239 (1970).
- 2) K. C. Nomura, *Phys. Rev. Lett.* **5**, 500 (1960).
- 3) S. Tutihasi, G. G. Roberts, R. C. Keezer, and R. E. Drews, *Phys. Rev.* **177**, 1143 (1969).
- 4) N. Miura and S. Tanaka, *phys. stat. sol.* **42**, 257 (1970).
- 5) R. Yoshizaki and S. Tanaka, *J. Phys. Soc. Jpn.* **30**, 1389 (1971).
- 6) L. Rothkirch, R. Link, W. Sauer, and F. Manglus, *phys. stat sol.* **31**, 147 (1969).
- 7) P. L. Weimer, *Proc. IEEE* **52**, 608 (1964).
- 8) H. L. Wilson and W. A. Gutierrez, *Proc. IEEE Lett.* **55**, 415 (1967).
- 9) J. Feinleib, J. deNeufville, S. C. Moss, and S. R. Ovshinsky, *Appl. Phys. Lett.* **18**, 254 (1971).
- 10) A. E. Bell and F. W. Spong, *Appl. Phys. Lett.* **38**, 920 (1981).
- 11) P. C. Clemens, *Appl. Opt.* **22**, 3165 (1983).
- 12) J. R. Reitz, *Phys. Rev.* **105**, 1233 (1957).
- 13) I. A. Firsov, *Soviet Phys. JETP* **5**, 1101 (1957).
- 14) T. Doi, K. Nakao, and H. Kamimura, *J. Phys. Soc. Jpn.* **28**, 36 (1970).
- 15) T. Doi, K. Nakao, and H. Kamimura, *J. Phys. Soc. Jpn.* **28**, 822 (1970).
- 16) K. Nakao, T. Doi, and H. Kamimura, *J. Phys. Soc. Jpn.* **30**, 1400 (1971).
- 17) E. L. Ivchenko and G. E. Pikus, *JETP Lett.* **27**, 604 (1978).
- 18) V. M. Asnin, A. A. Bakun, A. M. Danishevskii, E. L. Ivchenko, G. E. Pikus, and A. A. Rogachev, *JETP Lett.* **28**, 74 (1979).
- 19) V. M. Asnin, A. A. Bakun, A. M. Danishevskii, E. L. Ivchenko, G. E. Pikus, and A. A. Rogachev, *Solid State Commun.* **30**, 565 (1979).
- 20) X. Wan, A. M. Turner, A. Vishwanath, and S. Y. Savrasov, *Phys. Rev. B* **83**, 205101 (2011).
- 21) M. Hirayama, R. Okugawa, S. Ishibashi, S. Murakami, and T. Miyake, *Phys. Rev. Lett.* **114**, 206401 (2015).
- 22) K. Nakazawa, T. Yamaguchi, and A. Yamakage, *Phys. Rev. Materials* **8**, L091601 (2024).
- 23) T. Furukawa, Y. Shimokawa, K. Kobayashi, and T. Itou, *Nat. Commun.* **8**, 954 (2017).
- 24) T. Furukawa, Y. Watanabe, N. Ogasawara, K. Kobayashi, and T. Itou, *Phys. Rev. Research* **3**, 023111 (2021).
- 25) G. L. J. A. Rikken and N. Avarvari, *Phys. Rev. B* **99**, 245153 (2019).
- 26) J. Ma, B. Cheng, L. Li, Z. Fan, H. Mu, J. Lai, X. Song, D. Yang, J. Cheng, Z. Wang, C. Zeng, and D. Sun, *Nat. Commun.* **13**, 5425 (2022).

- 27) C. Niu, S. Huang, N. Ghosh, P. Tan, M. Wang, W. Wu, X. Xu, and P. D. Ye, *Nano Lett.* **23**, 3599 (2023).
- 28) M. D. Moldavskaya, L. E. Golub, S. N. Danilov, V. V. Bel'kov, D. Weiss, and S. D. Ganichev, *Phys. Rev.* **108**, 235209 (2023).
- 29) T. Satoh, S.-J. Cho, R. Iida, T. Shimura, K. Kuroda, H. Ueda, Y. Ueda, B. A. Ivanov, F. Nori, and M. Fiebig, *Phys. Rev. Lett.* **105**, 077402 (2010).
- 30) T. Satoh, Y. Terui, R. Moriya, B. A. Ivanov, K. Ando, E. Saitoh, T. Shimura, and K. Kuroda, *Nat. Photon.* **6**, 662 (2012).
- 31) W.-H. Hsu, K. Shen, Y. Fujii, A. Koreeda, and T. Satoh, *Phys. Rev. B* **102**, 174432 (2020).
- 32) K. Ishito, H. Mao, K. Kobayashi, Y. Kousaka, Y. Togawa, H. Kusunose, J. Kishine, and T. Satoh, *Chirality* **35**, 338 (2023).
- 33) K. Ishito, H. Mao, Y. Kousaka, Y. Togawa, S. Iwasaki, T. Zhang, S. Murakami, J. Kishine, and T. Satoh, *Nat. Phys.* **19**, 35 (2023).
- 34) R. C. Roca, N. Nishizawa, K. Nishibayashi, and H. Munekata, *J. Appl. Phys.* **123**, 213903 (2018).
- 35) N. Nishizawa, K. Nishibayashi, and H. Munekata, *Proc. Natl. Acad. Sci. U.S.A.* **114**, 1783 (2017).
- 36) It has been defined as *photovoltaic* tensor in B. I. Sturman and V. M. Fridkin, *The Photovoltaic and Photorefractive Effects in Noncentrosymmetric Materials*, Chapter 1 (Translated from the Russian by J.E.S. Bradley, Gordon and Breach Science Publishers S. A., 1992).
- 37) Irradiation area on a sample is estimated based on nominal beam diameter of 0.3 mm, with distance between a collimator and a sample of 100 mm and beam dispersion angle of 0.04° . Range of Bragg's angle is determined by a two-dimensional x-ray detector with solid angle of 26° . Distance between a sample and a detector is 200 mm.
- 38) J. S. Blakemore, J. W. Schultz, and K. C. Nomura, *J. Appl. Phys.* **31**, 2226 (1960).
- 39) T. Vasileiadis and S. Yannopoulos, *J. Appl. Phys.* **116**, 103510 (2014).
- 40) Coating of a SiO₂ layer was carried out without intentionally heating a sample holder. Power of RF sputtering was 100W with Ar atmosphere pressure of 1.0 Pa. Deposition rate was around 7.9 nm/min.
- 41) A. S. Pine and G. Dresselhaus, *Phys. Rev. B* **4**, 356 (1971).
- 42) S. Ji, T. Hayakawa, N. Suyama, K. Nakada, and A. Yamada, *Jpn. J. Appl. Phys.* **59**, 041003 (2020).

- 43) R. W. Boyd, *Nonlinear Optics*, p. 46, Table 1.5.2 (4th Ed., Academic Press, 2020).
- 44) F. Hennerberger, N. S. Averkiev, and R. J. Rasulo, *phys. stat. sol. (b)* **109**, 343 (1982).
- 45) J. W. McIver, D. Hsieh, H. Steinberg, P. Jarillo-Herrero, and N. Gedik, *Nat. Nanotechnol.* **7**, 96 (2012).
- 46) Polarization-dependent reflectivity R at $\theta = 45^\circ$ is estimated to be around 0.40 and 0.61 for $\mathbf{E} \parallel \mathbf{z}$ and $\mathbf{E} \perp \mathbf{z}$ at around 1.5 eV, respectively, on basis of dielectric constants of $\epsilon_1 \sim 40$ and 34, respectively, extracted by the work the Ref. 3.
- 47) S. S. Tsirkin, P. A. Puente, and I. Souza, *Phys. Rev. B* **97**, 035158 (2018).

Figure Captions

Figure 1: Schematic illustrations of (a) a part of a right-handed, trigonal wire made of Te atoms, and (b) a cross-sectional view of trigonal wires packed into a hexagonal array. These figures are prepared referring to Ref. 1 with permission from Wiley. (c) Definition of crystallographic axes used in this work. Three primitive axes in a hexagonal crystal are denoted by [100], [010], and [001] in terms of Miller indices, whereas a set (x, y, z) represents the orthogonal coordinate system used in the present study. Note: the [120] direction is parallel to the y axis.

Figure 2: Pole figures obtained at two different Bragg's angles with center values $2\theta_B$: (a) 23.1° and (b) 27.7° . Three auxiliary figures depicted on the right sides of pole figures are (c) a top view picture of a mother piece added with a red arrow which indicates incidence direction of an X-ray beam at $\varphi = 0^\circ$, (d) a hexagonal prism with the (010) plane and the [120] direction in pale blue, and (e) a hexagonal prism with the (011) plane and the [001] direction in orange. Symbols φ and ψ represent in-plane rotation and tilt angle of a sample stage relative to the incident X-ray plane. Symbols "a" to "f" on pole figures represent six different reflection planes.

Figure 3: (a) A top view picture of a mother piece which is cut into four quadrilateral-shaped chips. Crystallographic axes of hexagonal Te are shown on upper left. Schematic illustrations of (b) top and (c) cross-sectional views of a quadrilateral-shaped device, incorporating various constituent materials in the device.

Figure 4: Raman spectra in (a) relatively low and (b) relatively high wavenumber regions. In panel (a), polarization states of backscattered and impinging light are expressed by the notation XX in which H and V denote horizontal- and vertical-linear polarization, respectively. Inset shows a top view picture of *SiO₂-coated* sample A on which a pair of electrodes is formed parallel to the in-plane z direction. (b) Spectra measured with HH condition at four different accumulated illumination times. Yellow hatches represent

wavenumber regions in which broad TeO₂ bands have been reported.³⁹⁾

Figure 5: (a) A top view picture of *SiO₂-coated* sample B, together with an illustration which schematically shows relation between **x**, **y**, and **z** axes and crystal axes expressed by the Miller indices. Note that [120] direction is parallel to the axis normal to a cleaved plane. (b) Schematic illustration of setup for polarization-dependent photocurrent measurement. LD: laser diode, ISO: isolator, OCH: optical chopper, PD: photo diode, M1 and M2: gold coated mirrors, Gls: glass, GTP: Gran-Taylor prism, QWP: quarter wave plate, ND: neutral density filter (13%), FL: focus lens ($L = 70$ or 100 mm), Cam: IR camera, Te: Te sample, SB: aluminum sample box, and CA: current amplifier. (c) A model illustrating estimation of photocurrent density. Labels *a*, *b*, and *c* represent a pair of electrodes, rectangle windows through which a current flows, and excitation region, respectively. Notations ϕ and d denote diameter of excitation spot and penetration depth of light, respectively. Black arrows represent a photocurrent flowing along the axis of interest.

Figure 6: Photocurrent data obtained from *as-cleaved* sample A as a function of QWP angle (φ_Q) measured after three different accumulated illumination time $t =$ (a) 2, (b) 7, and (c) 11 h. A pair of electrodes is formed parallel to the *z* direction, as shown in inset Fig. 4 (a). Incident angle of light is $\theta = 45^\circ$ with *p*-polarization at $\varphi_Q = 0^\circ$, and excitation power density was 40.1 W/cm^2 . Notations P, L, and R, indicate *p*, left-circular, and right-circular polarizations, respectively. Red curved lines are for eye guide.

Figure 7: (a) Photocurrent data obtained from *SiO₂-coated* sample B as a function of rotation angle of QWP (φ_Q). Measurements were performed after total illumination time of $t = 5.5$ h at two different light-incident angles $\theta = 0$ and 45° , with pairs of electrodes (a) parallel and (b) perpendicular to the *z* direction. Initial polarization at $\varphi_Q = 0^\circ$ is *p*-polarizations with excitation power density 1.7 W/cm^2 . Notations P, L, and R, indicate *p*, left-circular, and right-circular polarizations, respectively. Red curved lines are for eye guide.

Figure 8: (a) A photocurrent curve in red calculated with Eq. (5) based on experimental data (black dots) shown in Fig. 7(a) with tilt angle $\theta = 45^\circ$. (b) Breakdown of a calculated photocurrent: CPGE component in a solid red line, LPGE component in a solid green line, and polarization-dependent absorption component in a dashed purple line. Notations P, L, and R, indicate p , left-circular, and right-circular polarizations, respectively.

Table 1: A list of four coefficients, C , L_1 , L_2 , and D extracted from five different experimental data through inverse analysis using Eq. (5). The first two digits indicate significant figures. Experimental data are those shown in, from the top row to the bottom row, Fig. 6(a), Fig. 6(b), Fig. 2S, Fig. 7(a), and Fig. 3S, respectively.

Sample ID	specification	measurement	C	L_1	L_2	D	C/D	L_2/D
A	as- cleaved	p , 40.1 W/cm ² , $t = 2$ hrs	3.56	7.71	13.3	238	0.015	0.056
	as- cleaved	p , 40.1 W/cm ² , $t = 7$ hrs	1.35	-3.17	6.24	145	0.009	0.043
	polished & SiO ₂ coated	p , 44.5 W/cm ² , $t = 7$ hrs	0.420	-1.45	2.27	25.1	0.017	0.090
B	polished & SiO ₂ coated	p 1.7 W/cm ² , $t = 5.5$ hrs	0.180	-0.178	0.979	12.5	0.014	0.078
	polished & SiO ₂ coated	s , 1.7 W/cm ² , $t = 10$ hrs	-0.020	0.0126	-0.225	5.55	-0.004	-0.041

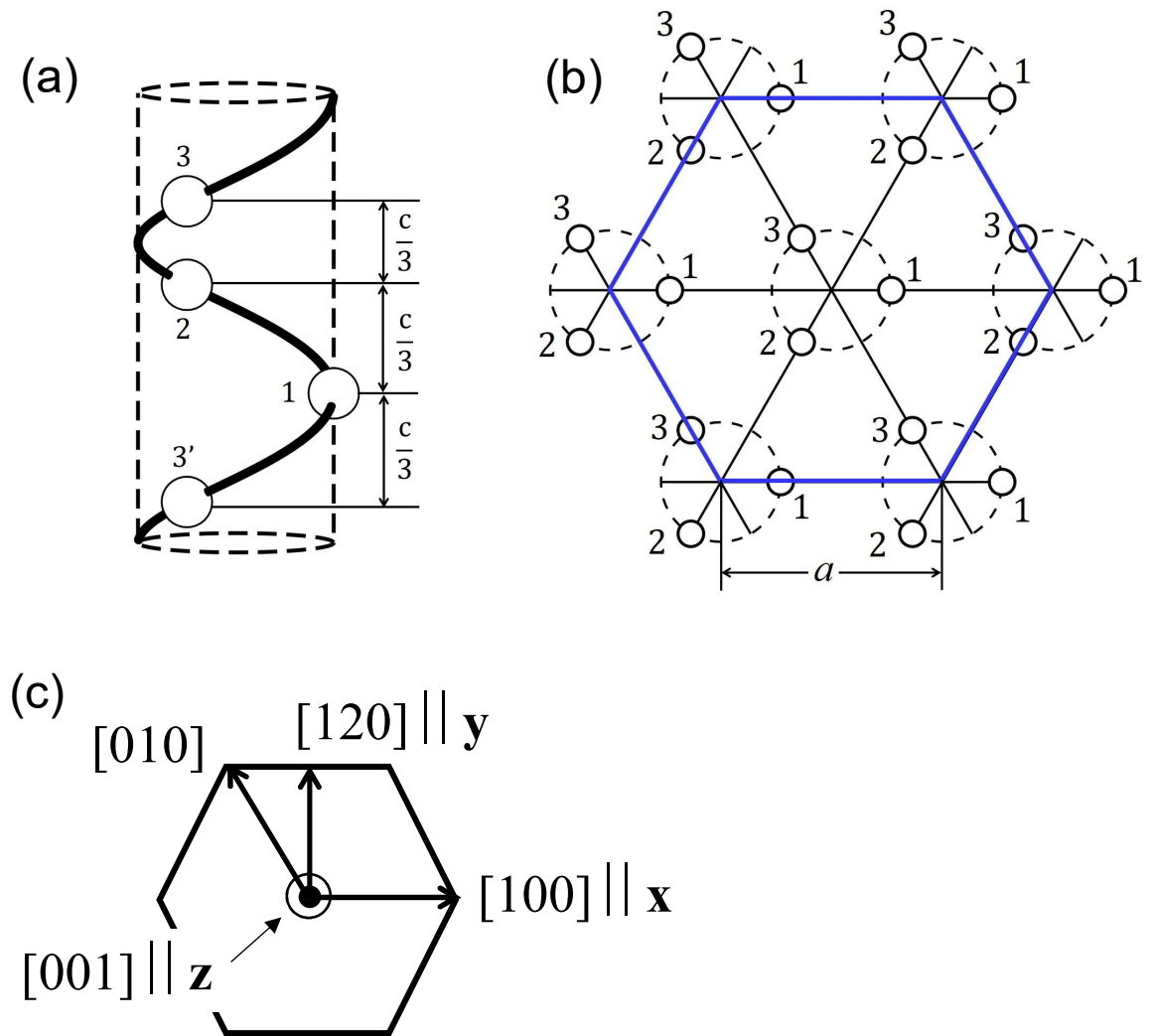


Figure 1: Schematic illustrations of (a) a part of a right-handed, trigonal wire made of Te atoms, and (b) a cross-sectional view of trigonal wires packed into a hexagonal array. These figures are prepared referring to Ref. 1 with permission from Wiley. (c) Definition of crystallographic axes used in this work. Three primitive axes in a hexagonal crystal are denoted by $[100]$, $[010]$, and $[001]$ in terms of Miller indices, whereas a set (x, y, z) represents the orthogonal coordinate system used in the present study. Note: the $[120]$ direction is parallel to the y axis.

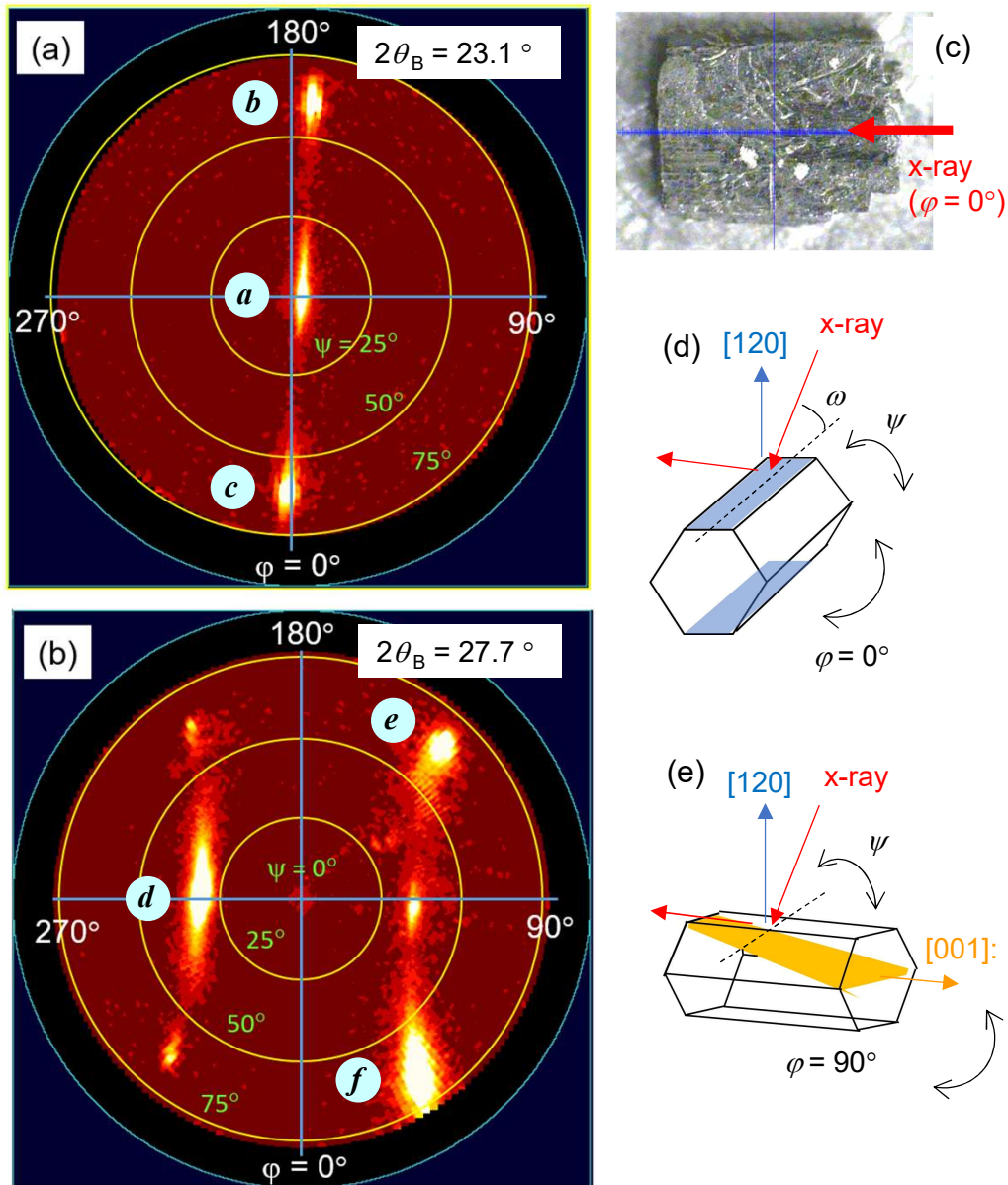


Figure 2: Pole figures obtained at two different Bragg's angles with center values $2\theta_B$: (a) 23.1° and (b) 27.7° . Three auxiliary figures depicted on the right sides of pole figures are (c) a top view picture of a mother piece added with a red arrow which indicates incidence direction of an X-ray beam at $\phi = 0^\circ$, (d) a hexagonal prism with the (010) plane and the [120] direction in pale blue, and (e) a hexagonal prism with the (011) plane and the [001] direction in orange. Symbols ϕ and ψ represent in-plane rotation and tilt angle of a sample stage relative to the incident X-ray plane. Symbols "a" to "f" on pole figures represent six different reflection planes.

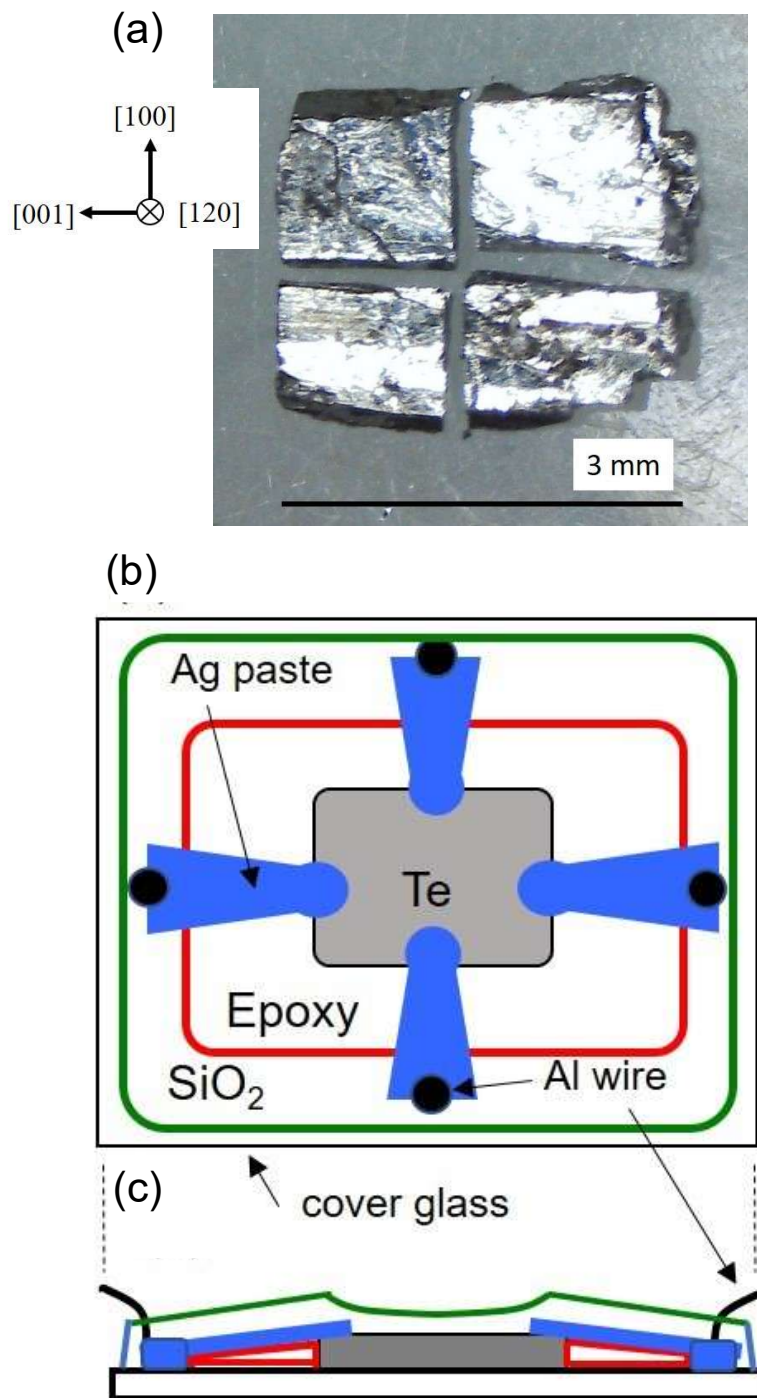


Figure 3: (a) A top view picture of a mother piece which is cut into four quadrilateral-shaped chips. Crystallographic axes of hexagonal Te are shown on upper left. Schematic illustrations of (b) top and (c) cross-sectional views of a quadrilateral-shaped device, incorporating various constituent materials in the device.

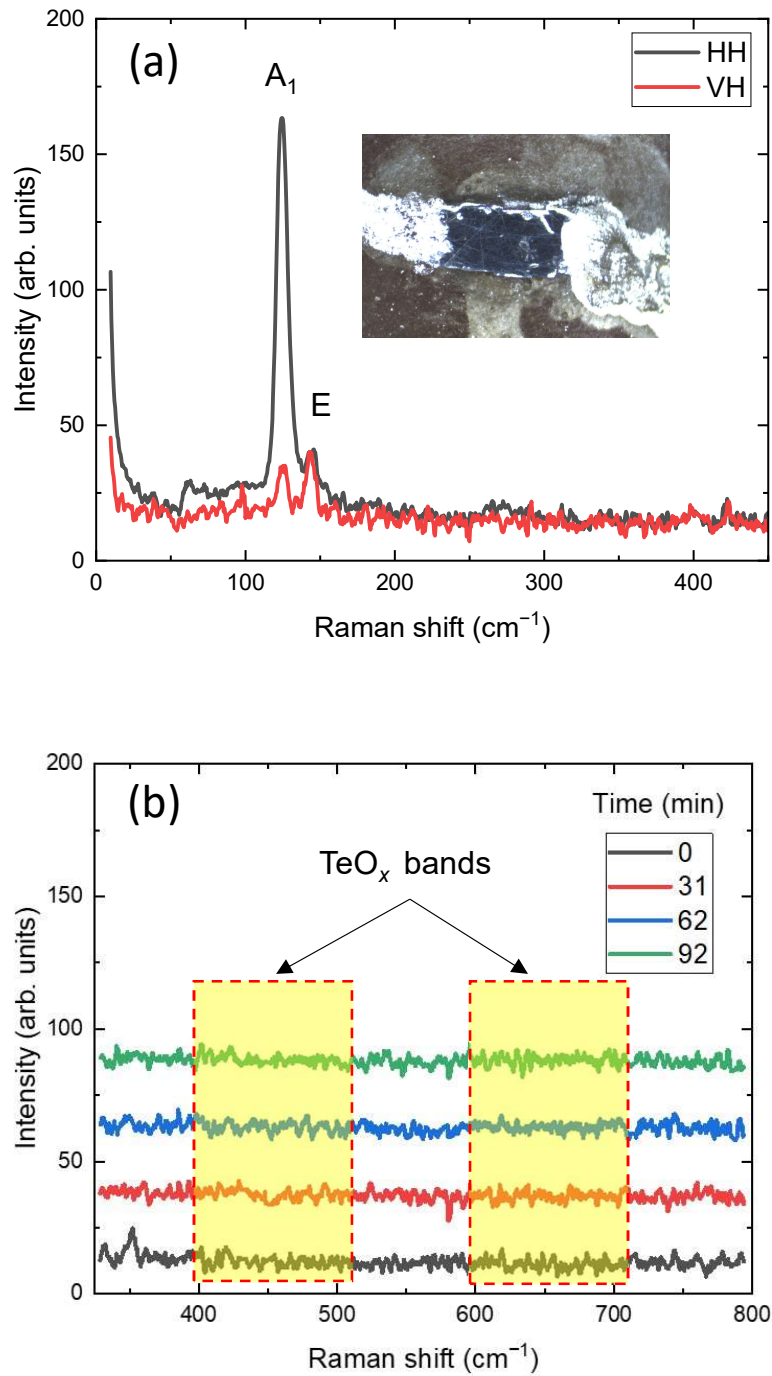


Figure 4: Raman spectra in (a) relatively low and (b) relatively high wavenumber regions. In panel (a), polarization states of backscattered and impinging light are expressed by the notation XX in which H and V denote horizontal- and vertical-linear polarization, respectively. Inset shows a top view picture of SiO_2 -coated sample A on which a pair of electrodes is formed parallel to the in-plane z direction. (b) Spectra measured with HH condition at four different accumulated illumination times. Yellow hatches represent wavenumber regions in which broad TeO_2 bands have been reported.³⁹⁾

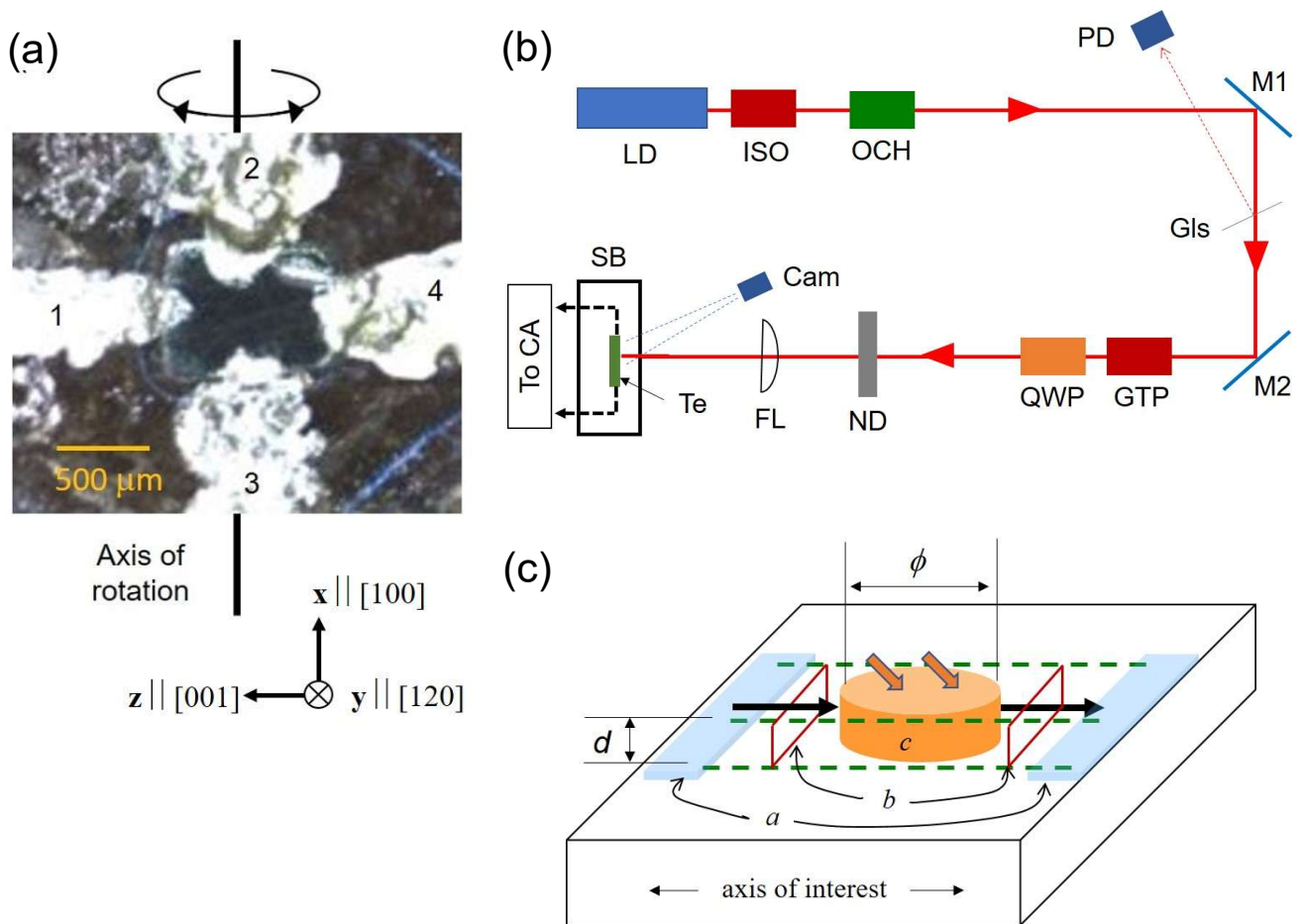


Figure 5: (a) A top view picture of SiO_2 -coated sample B, together with an illustration which schematically shows relation between x , y , and z axes and crystal axes expressed by the Miller indices. Note that $[120]$ direction is parallel to the axis normal to a cleaved plane. (b) Schematic illustration of setup for polarization-dependent photocurrent measurement. LD: laser diode, ISO: isolator, OCH: optical chopper, PD: photo diode, M1 and M2: gold coated mirrors, Gls: glass, GTP: Gran-Taylor prism, QWP: quarter wave plate, ND: neutral density filter (13%), FL: focus lens ($L = 70$ or 100 mm), Cam: IR camera, Te: Te sample, SB: aluminum sample box, and CA: current amplifier. (c) A model illustrating estimation of photocurrent density. Labels a , b , and c represent a pair of electrodes, rectangle windows through which a current flows, and excitation region, respectively. Notations ϕ and d denote diameter of excitation spot and penetration depth of light, respectively. Black arrows represent a photocurrent flowing along the axis of interest.

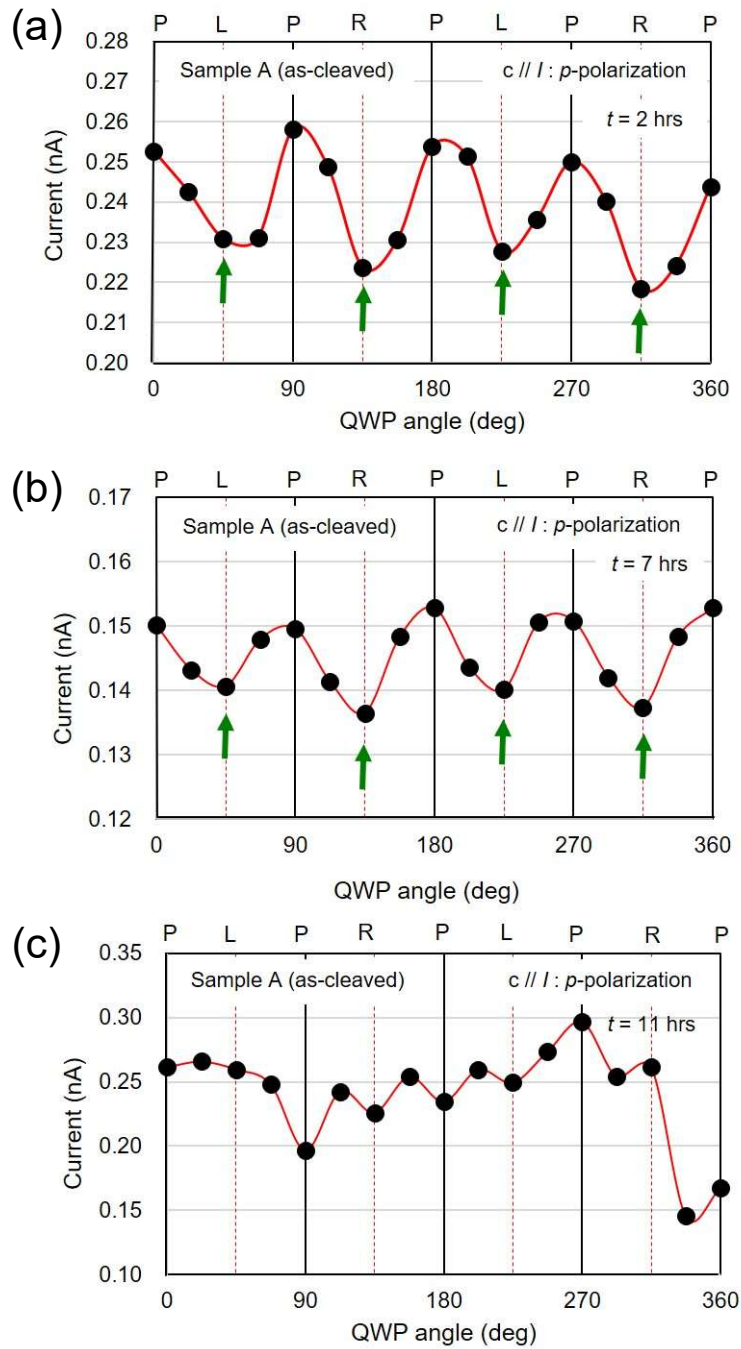


Figure 6: Photocurrent data obtained from *as-cleaved* sample A as a function of QWP angle (φ_Q) measured after three different accumulated illumination time $t =$ (a) 2, (b) 7, and (c) 11 h. A pair of electrodes is formed parallel to the z direction, as shown in inset Fig. 4 (a). Incident angle of light is $\theta = 45^\circ$ with p -polarization at $\varphi_Q = 0^\circ$, and excitation power density was 40.1 W/cm^2 . Notations P, L, and R, indicate p , left-circular, and right-circular polarizations, respectively. Red curved lines are for eye guide.

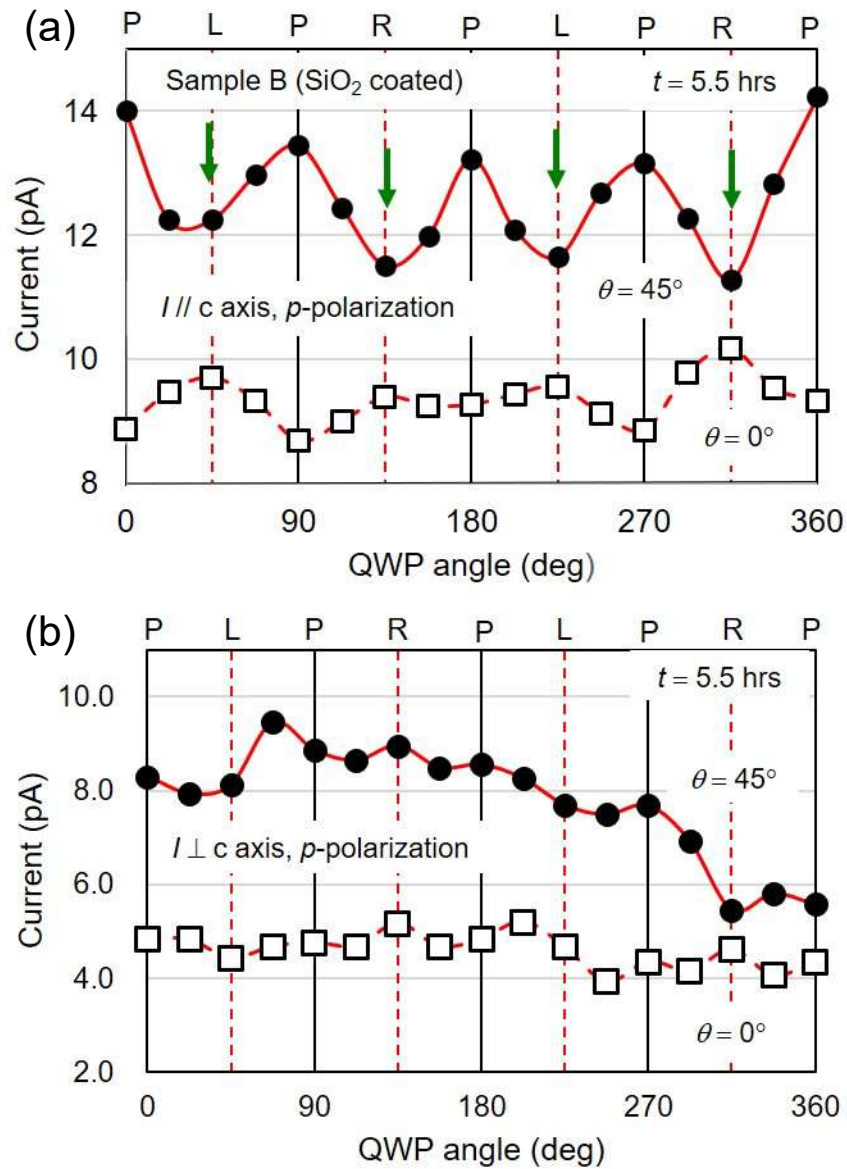


Figure 7: (a) Photocurrent data obtained from SiO_2 -coated sample B as a function of rotation angle of QWP (φ_Q). Measurements were performed after total illumination time of $t = 5.5$ h at two different light-incident angles $\theta = 0$ and 45° , with pairs of electrodes (a) parallel and (b) perpendicular to the z direction. Initial polarization at $\varphi_Q = 0^\circ$ is p -polarizations with excitation power density 1.7 W/cm^2 . Notations P, L, and R, indicate p , left-circular, and right-circular polarizations, respectively. Red curved lines are for eye guide.

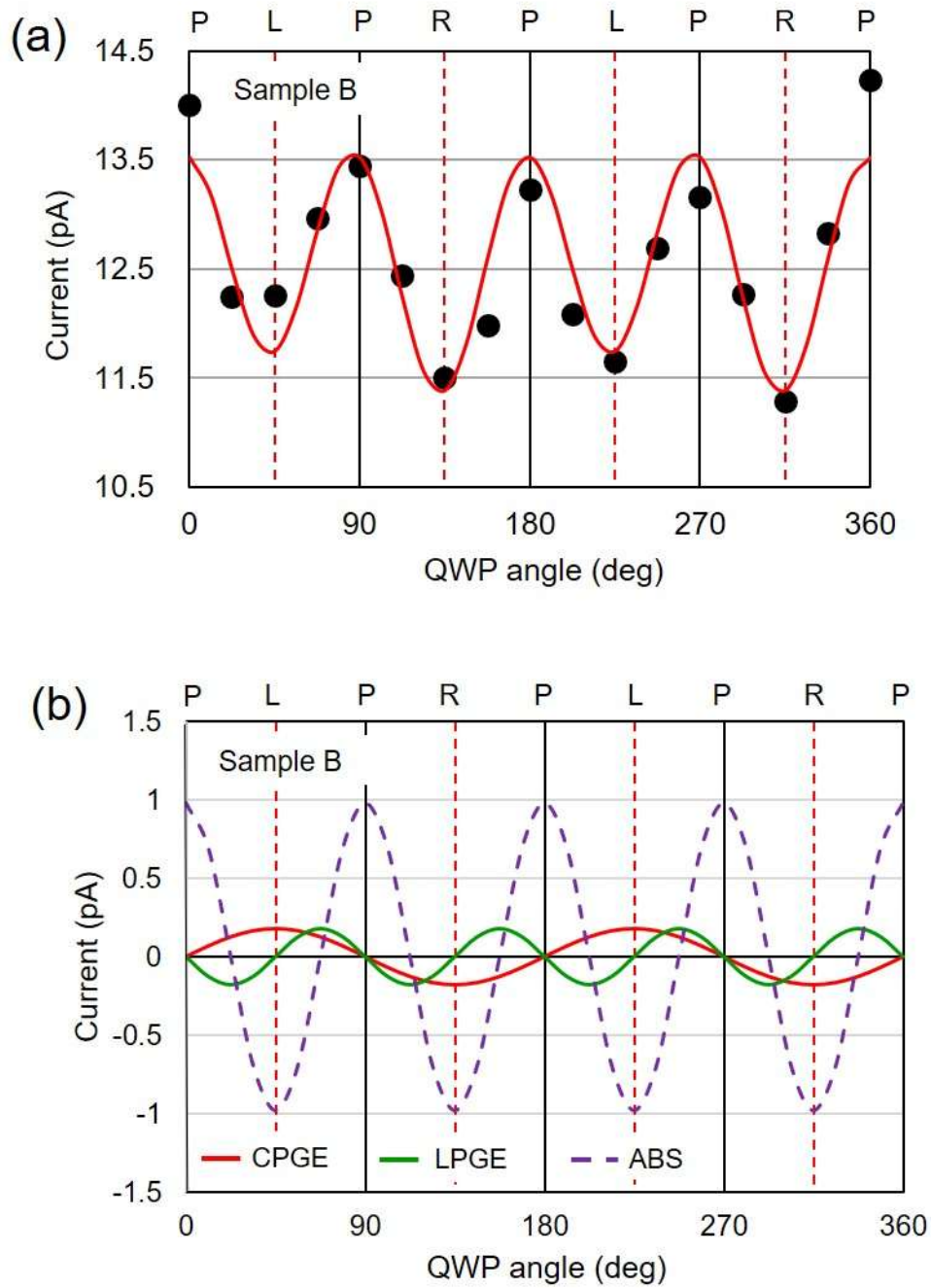


Figure 8: (a) A photocurrent curve in red calculated with Eq. (5) based on experimental data (black dots) shown in Fig. 7(a) with tilt angle $\theta = 45^\circ$. (b) Breakdown of a calculated photocurrent: CPGE component in a solid red line, LPGE component in a solid green line, and polarization-dependent absorption component in a dashed purple line. Notations P, L, and R, indicate p , left-circular, and right-circular polarizations, respectively.